Second harmonic generation control in twisted bilayers of transition metal dichalcogenides

Ioannis Paradisanos,[1,*] Andres Manuel Saiz Raven,[1] Thierry Amand,[1] Cedric Robert,[1] Pierre Renucci,[1] Kenji Watanabe,[2] Takashi Taniguchi,[3] Iann C. Gerber,[1] Xavier Marie,[1] and Bernhard Urbaszek[1,†]

[1]*Université de Toulouse, INSA-CNRS-UPS, LPCNO, 135 Avenue Rangueil, 31077 Toulouse, France*

[2]*Research Center for Functional Materials, National Institute for Materials Science, 1-1 Namiki, Tsukuba 305-0044, Japan*

[3]*International Center for Materials Nanoarchitectonics, National Institute for Materials Science, 1-1 Namiki, Tsukuba 305-0044, Japan*

(Received 26 October 2021; revised 18 February 2022; accepted 23 February 2022; published 18 March 2022)

The twist angle in transition metal dichalcogenide heterobilayers is a compelling degree of freedom that determines electron correlations and the period of lateral confinement of moiré excitons. Here we perform polarization-resolved second harmonic generation (SHG) spectroscopy of MoS_2/WSe_2 heterostructures. We demonstrate that by choosing suitable laser energies the twist angle between two monolayers can be measured directly on the assembled heterostructure. We show that the amplitude and polarization of the SHG signal from the heterostructure are determined by the twist angle between the layers and exciton resonances at the SH energy. For heterostructures with close to zero twist angle, we observe changes of exciton resonance energies and the appearance of new resonances in the linear and nonlinear susceptibilities.

DOI: 10.1103/PhysRevB.105.115420

I. INTRODUCTION

The optical and electronic properties of van der Waals (vdW) materials can be tuned by adjusting the twist angle for bilayer heterostructures [1,2]. A moiré superlattice forms by stacking two transition metal dichalcogenide (TMD) monolayers with a finite twist angle and/or different lattice constants [3]. This periodic pattern can host new quantum phenomena in two-dimensional heterostructures [4] and homobilayers. Correlated states and superconductivity are investigated in twisted bilayer graphene [5] and TMDs [6–9], interlayer excitons trapped in strain-induced [10] and moiré [11–13] potentials, hybridization of excitons [14–17] and first hints of collective phenomena such as condensation [18–20].

Nonlinear optics describes the interaction of photons within a nonlinear medium [21]. In the limit of high light intensities, second harmonic generation (SHG) can emerge where two photons of identical energy combine into one photon of twice this energy [22,23]. Potassium dihydrogen phosphate and lithium niobate ($LiNbO_3$) [24] are two widely known examples of crystals for SHG applications in photonics and laser physics. Other applications include II-VI and III-V semiconductors [25–28], magnetic- and nonmagnetic layered materials [29–35], nanotubes [36], and antiferromagnetic oxides and perovskites [37,38].

Polarization-resolved SHG measurements (PSHG) allows determining the crystallographic orientation of monolayers, as well as the twist angle and charge transfer dynamics in bilayer heterostructures [39–45]. The SHG intensity reaches a maximum value when the electric field vector of the excitation laser beam is parallel to the armchair orientation of TMD monolayers according to the nonlinear susceptibility tensor $\chi^{(2)}$ of the D_{3h} point group [46,47].

The twist angle between two monolayers in a heterostructure is usually measured by PSHG experiments on the constituent monolayers and not on the heterostructure region itself [10,12,44,48,49]. This approach has several drawbacks, as monolayer drift and rotation are possible during the assembly process. In addition, strain and lattice reconstruction can naturally occur due to the interaction between the layers [9,50], depending on the twist angle and lattice mismatch between the monolayers [1,51]. Direct information from the assembled bilayer region is therefore needed.

Here, we perform SHG spectroscopy and PSHG with a tunable laser on several MoS_2/WSe_2 heterostructures with different twist angles. Our target is to obtain information from the individual layers in the already assembled device in order to control the overall SHG response. The investigated heterobilayer system is relevant for optoelectronic applications extending to the infrared and also as a versatile platform for moiré physics [52–56]. We vary the fundamental laser energy (E_L) and we collect the amplitude of the SHG in the energy range across the A and B exciton states. The energies presented in this work correspond to twice the fundamental laser energy ($2 \times E_L$). We tune the interference between the SHG signals from the constituent monolayers. We show that the contribution of each monolayer to the global SHG signal from the bilayer strongly depends on energy: For the individual monolayers, we observe orders of magnitude enhancement of the SHG intensity when twice the laser excitation energy is

*paradeis@insa-toulouse.fr
†urbaszek@insa-toulouse.fr

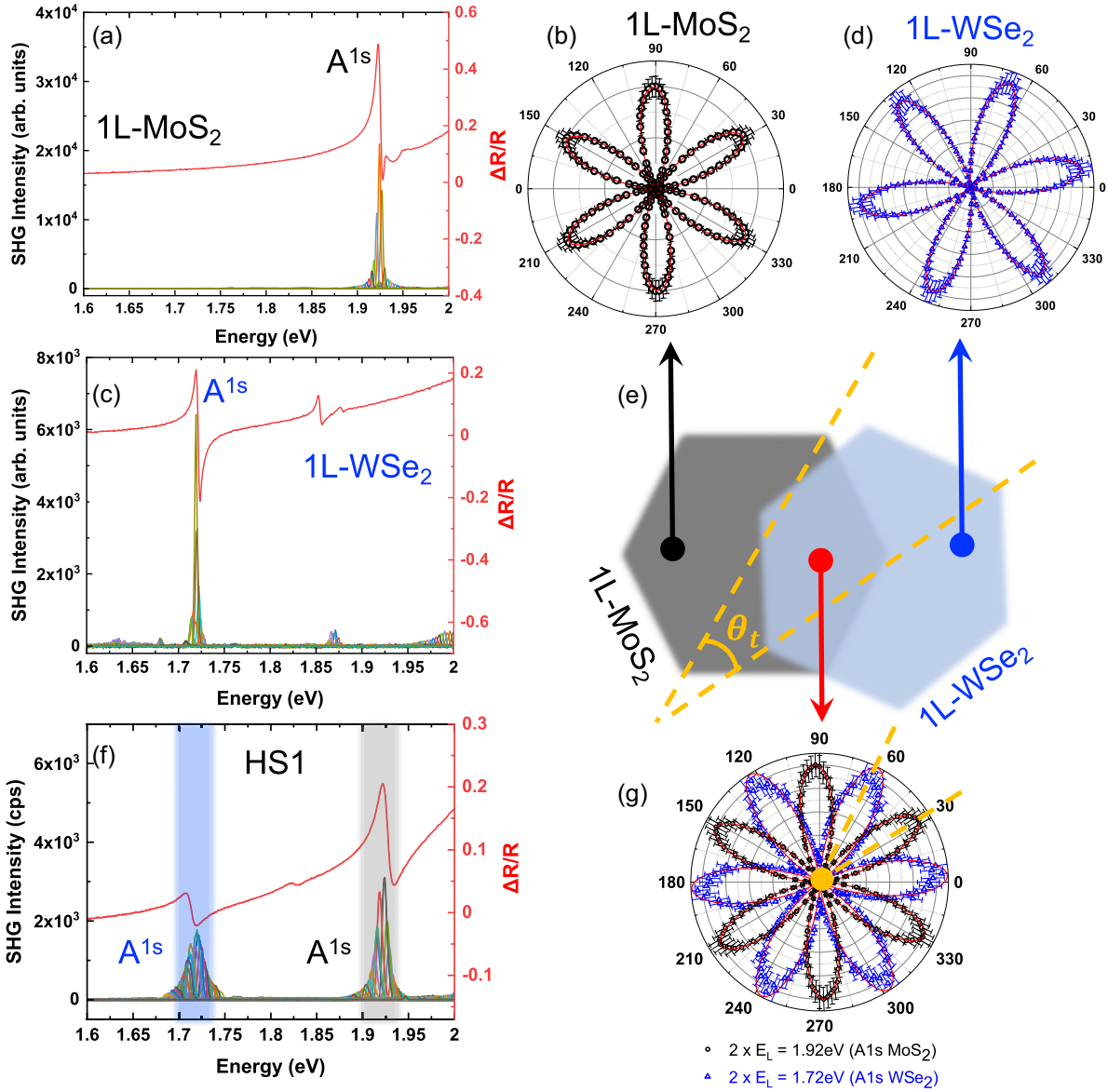

FIG. 1. SHG spectroscopy on monolayers and heterostructure region. (a) Differential reflectivity (red line) and wavelength-dependent SHG of 1L-MoS_2. For the SHG spectra, the energy in the x axis corresponds to twice the fundamental laser energy ($2 \times E_L$). (b) Polar plot of SHG in 1L-MoS_2 at $2 \times E_L = 1.92$ eV. We measure over an angle range of 120° and generate the rest of the plot by repeating the data. (c) Same as panel (a) but for 1L-WSe_2. (d) Same as panel (b) but at $2 \times E_L = 1.72$ eV in 1L-WSe_2. (e) Schematic drawing of the different areas of the heterostructure with access also to monolayer regions. The twist angle θ_t is indicated. (f) Same as panels (a) and (c) but for the heterostructure region. (g) Polar plots for the heterostructure region but at two *different* values of E_L: blue triangles for $2 \times E_L = 1.72$ eV and black circles for $2 \times E_L = 1.92$ eV. All the polar plots are fitted with a $\cos^2 3(\theta - \theta_0)$ function (red lines), where θ is the angle of the pump laser polarization and θ_0 is a free parameter to extract the armchair orientation with respect to the laboratory axis (here the x axis).

tuned to the A1s exciton of each monolayer alone (these resonances are well separated in energy: 1.72 eV for monolayer WSe_2, 1.92 eV for MoS_2).

When investigating the heterobilayer with a twist angle θ_t, by varying the laser energy, we distinguish three main scenarios.

(i) The SHG signal from the bilayer is dominated by WSe_2 at $2 \times E_L = 1.72$ eV, as the MoS_2 SHG contribution at this energy is orders of magnitude weaker.

(ii) At $2 \times E_L = 1.92$ eV, the SHG from the heterobilayer is dominated by MoS_2 and the WSe_2 contribution is negligible.

(iii) When $2 \times E_L$ is in resonance with a continuum of states from the heterobilayer band structure, the SHG signal of the bilayer can be seen as the interference of two plane waves.

This approach based on tuning $2 \times E_L$ to different exciton resonances allows accessing information on the crystallographic orientation of the individual monolayers in a heterostructure; i.e., our experiments allow us to extract information on twist planes in an assembled vdW stack [57].

For the heterostructure sample with close to 0° twist angle we observe enhancement in the SHG intensity at very different exciton resonance energies as compared to the large twist

angle sample, possibly linked to strain, the hybridization of the electronic states, or the formation of moiré minibands [49,52,58–60]. We believe our results can be directly applicable to many multilayer systems with distinct exciton states [1].

II. RESULTS

We investigate three heterobilayers, HS1–HS3, with different twist angles θ_t between WSe_2 and MoS_2. The structures share the same MoS_2 monolayer and the same hexagonal Boron Nitride (hBN) encapsulation (top and bottom) to allow isolating changes due to the twist angle only (see schematics in Fig. 1(e) and Supplemental Material A for optical microscope image [61]). For SHG spectroscopy we use a pulsed Ti:sapphire laser source coupled to an optical parametric oscillator (OPO) and we scan the fundamental laser energy (i.e., E_L) over the energy range that the SHG corresponds to the main optical transitions. Experiments are performed at a temperature of $T = 5$ K in vacuum in a confocal microscope (excitation/detection spot diameter of the order of the wavelength) (see Ref. [2] and Methods).

A. SHG comparison monolayers versus heterobilayers

In Figs. 1(a) and 1(c) we plot SHG spectra from the MoS_2 and WSe_2 monolayers for laser energies between $2 \times E_L =$ 1.6 to 2 eV in steps of ≈3 meV between two adjacent spectra. Each SHG spectrum is composed of a single peak that corresponds to a separate data acquisition for each excitation laser energy E_L (see Supplemental Material B for experimental details on SHG spectroscopy [61]) [62]. For 1L-MoS_2 the SHG amplitude is strongly enhanced at 1.92 eV, and for 1L-WSe_2 it is strongly enhanced at 1.72 eV. Comparing SHG spectra with white light reflectivity (see Methods) plotted in the same panels in Figs. 1(a) and 1(c), we conclude that the maxima in the SHG amplitude occur when $2 \times E_L$ is resonant with intralayer A excitons (i.e., Coulomb-bound electron-hole pairs within the same layer) [33,63]. The excitonic contribution to the SHG intensity can be orders of magnitude higher than the intrinsic contribution from the crystal, as reported for TMD monolayers and other material systems [27,32,37,64–67]. It has been suggested that the D_{3h} point symmetry of TMD monolayers leads to a mixing between s- and p-shell excitons making them active in both single- and two-photon processes [65].

For the MoS_2 monolayer we perform PSHG at the A-exciton resonance ($2 \times E_L = 1.92$ eV) to extract the crystallographic orientation [see Fig. 1(b)]. We measure the SHG amplitude as a function of the linearly polarized excitation angle with respect to the in-plane crystallographic orientation (see Supplemental Material C for details on PSHG [61]) and we present the results in a polar plot in Fig. 1(b). We repeat the corresponding experiment for the WSe_2 monolayer by tuning now the laser energy in resonance with the corresponding A exciton ($2 \times E_L = 1.72$ eV) and perform PSHG [see polar plot in Fig. 1(d)]. For both PSHG measurements on monolayers the measured SHG integrated intensity modulation can be fitted with a $\cos^2 3(\theta - \theta_0)$ function, where θ is the angle of the laser polarization and θ_0 is a free parameter to extract the armchair orientation with respect to the laboratory axis (here the x axis) [68]. Based on the relative armchair orientation, we determine a twist angle ($\theta_t = 21.45 \pm 0.39^\circ$) between the individual monolayers (see Supplemental Material C for a discussion on the error bars [61]).

For the measurements in Fig. 1(f), we place the excitation/detection spot on the heterobilayer region of HS1 where MoS_2 and WSe_2 overlap [see red arrow in Fig. 1(e)], and we perform SHG spectroscopy. The results in Fig. 1(f) show strong resonances at the energies of the intralayer A exciton of WSe_2 (1.72 eV) and MoS_2 (1.92 eV), respectively. Note that the overall nonlinear response of the A-excitonic resonances appears broader in the heterostructures [full width at half maximum (FWHM) ≈ 15 meV, see Fig. 1(f)] compared to the bare monolayers [FWHM ≈5 meV, see Figs. 1(a) and 1(b)]. This can be due to fast charge transfer processes due to the type-II band alignment [69] or/and disorder (i.e., strain, impurities) introduced by the additional transfer steps.

In a second step, we tune $2 \times E_L$ on the WSe_2 intralayer exciton resonance and we perform PSHG [see blue data points in Fig. 1(g)]. Then we change the laser energy to $2 \times E_L = 1.92$ eV and perform PSHG experiments [see black data points in Fig. 1(g)]. Comparing the two data sets we see two very distinctive polar plots using two different values of E_L, although we carried out the measurements at the same spot of the heterobilayer. We extract a twist angle of $\theta_t = (29.82 \pm 0.41)^\circ$ between the two polar plots in Fig. 1(g), an angle slightly larger than determined for the separate monolayer orientations, possibly indicating a rotation of the WSe_2 layer during the assembly process (see Supplemental Material D for discussion on the angle mismatch [61]). If we compare the PSHG from the heterobilayer with the monolayer measurements, we find that for the heterostructure the WSe_2 contribution totally dominates at $2 \times E_L = 1.72$ eV, whereas at $2 \times E_L = 1.92$ eV the MoS_2 contribution is predominant (see more quantitative analysis in the Sec. III). The intralayer A-exciton states of WSe_2 and MoS_2 have a distinct contribution in the SHG response of the heterostructure. As a result, for certain energies one of the two constituent monolayers will exclusively contribute to the SHG signal. So by varying the laser energy on an already assembled heterostructure we can determine *in situ* the crystallographic direction of the constituent layers. This has important implications, as the twist angle determines band structures and hence electrical and optical properties.

We did not scan the lower energy range for interlayer excitons, as in SHG spectroscopy and linear absorption mainly direct transitions with high oscillator strength are visible.

B. SHG spectroscopy for heterobilayers with different twist angles

Our next target is to investigate the SHG response as a function of twist angle as shown in Fig. 2 for three different heterostructures. We show in Fig. 2(a) an extended scan of the results from Fig. 1(f) on HS1. We reveal at energies $2 \times E_L >$ 2.05 eV an onset of a continuum of states. In Fig. 2(b) we cover the same energy range but investigate a different WSe_2 layer on top of MoS_2 in HS2 (see Supplemental Material A for sample images [61]). We perform for HS2 PSHG at $2 \times E_L =$

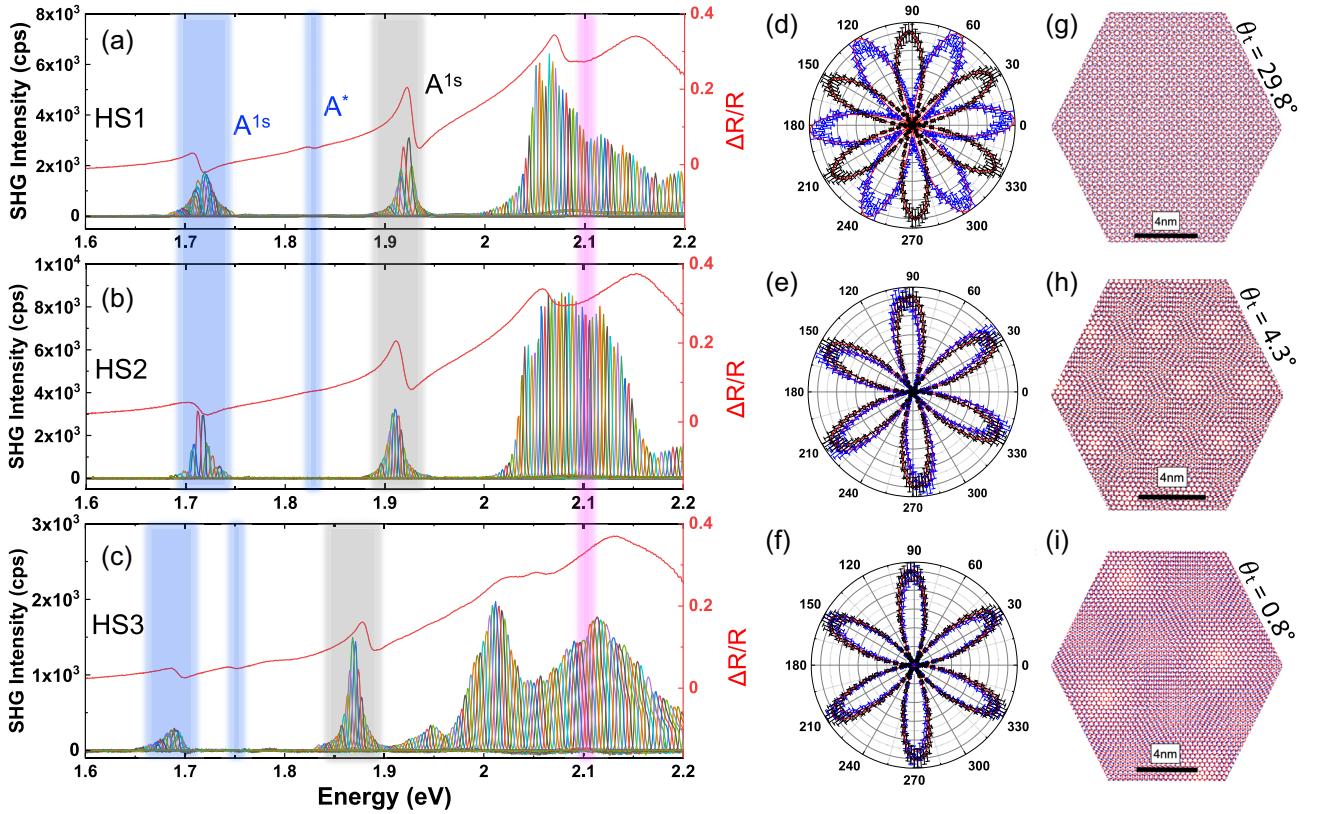

FIG. 2. SHG spectroscopy and polarization-resolved SHG for three different MoS_2/WSe_2 heterostructures. From top to bottom: Differential reflectivity (red lines) and wavelength-dependent SHG of (a) HS1 studied in Fig. 1, (b) HS2, and (c) HS3. For the SHG spectra, the energy in the x axis corresponds to twice the fundamental laser energy ($2 \times E_L$). The A-exciton states of MoS_2 and WSe_2 are indicated with black and blue shaded regions, respectively. The respective polar plots when twice the excitation energy is in resonance with the corresponding A excitons of MoS_2 (black) and WSe_2 (blue) are shown in panels (d), (e), and (f). Schematic representation of the moiré pattern of 1L-MoS_2/1L-WSe_2 heterostructures with twist angles θ_t of (g) HS1 $= 29.8°$, (h) HS2 $= 4.3°$, and (i) HS3 $= 0.8°$. The extracted moiré period is 0.62, 3.84, and 8.45 nm, respectively. Regions with main excitonic transitions are shaded blue and gray. A magenta stripe is shown at 2.1 eV to indicate $2 \times E_L$ used for the experiments presented in Fig. 3.

1.72 eV [blue data in Fig. 2(e)] and $2 \times E_L = 1.92$ eV [black data in Fig. 2(e)]. Also for HS2 we obtain two very different angle dependencies at these different laser energies. This allows us to extract *in situ* a twist angle between the layers of $\theta_t = (4.33 \pm 0.51)°$, in very good agreement with the twist angle extracted from the orientation of the monolayer parts outside the heterostructure region (see Supplemental Material D [61]). The SHG spectroscopy results obtained throughout these studies for HS1 and HS2 are very consistent in terms of exciton resonances and continuum onset; the different twist angle θ_t is the most striking difference between HS1 and HS2.

In Figs. 2(g)–2(i) we plot monolayer WSe_2 on top of monolayer MoS_2 for different twist angles in an idealized lattice configuration (ignoring lattice reconstruction). By considering the lattice mismatch between MoS_2 and WSe_2, we graphically extract the periodicity of the moiré superlattice to be 0.62 and 3.8 nm for twist angles that correspond to HS1 and HS2, respectively. Interestingly, due to the large lattice mismatch of 3.7%, also a zero degree twist angle results, in principle, in the formation of a periodic moiré landscape (period ≈8.5 nm). Quantum-confined electronic states and moiré patterns in MoS_2/WSe_2 heterobilayers have been observed previously using spectroscopy techniques and electron microscopy [52,55].

For HS3 with close to zero twist angle, we measure a very different response in linear and nonlinear optics as compared to the larger twist angle samples, namely, (i) in both differential reflectivity and SHG spectroscopy the main resonances are strongly red-shifted by 40 meV, and (ii) for HS3 in the energy range $2 \times E_L$ from 1.9 to 2.05 eV a strong SHG signal amplitude is recorded. In contrast, over this energy range the signal for the other structures HS1 and HS2 is close to zero. Both observations indicate that the band structure for HS3 is altered as compared to HS1 and HS2. In order to perform PSHG on intralayer excitons, we tune the laser energy to the red-shifted resonance energies at 1.68 and 1.88 eV clearly visible in Fig. 2(c); the corresponding angle-dependent data are plotted in Fig. 2(f). As expected for a sample with close to zero (or 60°) twist angle, the two sets of data are oriented along the same axis. As for HS3, we find an SHG signal amplitude that is, in general, roughly equal to the sum of the measured monolayer SHG amplitudes (for $2 \times E_L = 2.1$ eV); we conclude that the zero degree twist angle corresponds to R-type and not H-type (i.e., 60°) stacking [39].

C. SHG polarization control

In addition to the main intralayer exciton resonances, we also investigated the SHG response at other energies that contain crucial information on the heterostructure. In Fig. 3 we plot the PSHG results for the measurements at $2 \times E_L =$ 2.1 eV in the continuum of states for HS1–HS3, indicated by a magenta stripe in Figs. 2(a)–2(c). The results are very different compared to the SHG close to intralayer exciton resonances: for HS1 we find that the signal is maximized along an axis that is neither aligned with MoS_2 nor with WSe_2, compare black and blue lines with magenta spheres in Fig. 3(a). Here, the black and blue dashed lines correspond to the armchair orientation of MoS_2 and WSe_2, respectively. A striking feature is that the signal does not go to zero, so we have a strongly changed minimum to maximum SHG signal ratio as a function of the polarization angle for this measurement. This is a signature of elliptically polarized SHG emission [43,70], in contrast to the linearly polarized SHG plotted in Figs. 2(d)–2(f) of the same heterobilayer sample but at lower laser energy.

For HS2, PSHG measurements also result in a slightly shifted polar plot as compared to the monolayer orientations, but now the minimum to maximum SHG signal ratio is close to zero, indicating close to linear polarization. From our measurements we determine an angle for the polarization maximum in-between the MoS_2 and WSe_2 armchair directions.

For HS3 close to zero twist angle [$\theta_t = (0.79 \pm 0.53)^\circ$], the PSHG results show linearly polarized light, and not elliptically polarized light. For the three heterostructures at $2 \times E_L = 2.1$ eV, we use the twist angle, individual layer contributions, and phase differences to fit the measured data with a very simple plane wave model [43] (see Sec. III).

III. DISCUSSION

First, we discuss for HS3 with $\theta_t = 0.8^\circ$ twist angle possible origins of the redshift of the main intralayer excitonic transitions and the appearance of new resonances, which still need further investigation. Comparing with the literature, our observations are in agreement with emergent moiré superlattice exciton states when the two lattices are closely aligned. This has been previously observed using reflectivity and photoluminescence excitation experiments in WS_2/WSe_2 heterostructures [49] where the lattice mismatch of 4% is very similar to that of MoS_2/WSe_2 with 3.7%. In a study that combines spectroscopy with density functional theory, a large in-plane strain variation across the moiré unit cell of the MoS_2/WSe_2 heterobilayer has been proposed [58], leading to energy shifts. The important role of strain for the MoS_2/WSe_2 heterobilayer is also shown when investigating interlayer exciton formation [60]. In reconstructed WSe_2/WS_2 moiré superlattices quantitative studies of moiré flat bands are reported by comparing scanning tunneling spectroscopy of high-quality exfoliated TMD heterostructure devices with *ab initio* simulations of TMD moiré superlattices. Also, in these studies large in-plane strain redistribution is identified in WSe_2/WS_2 moiré heterostructures linked to

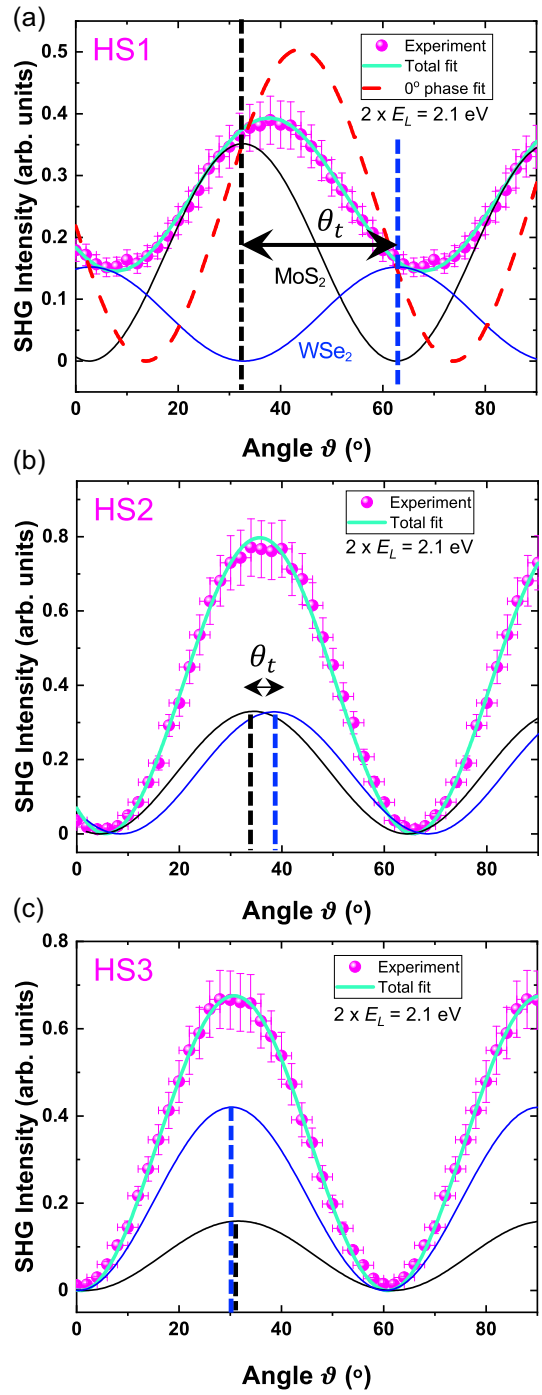

FIG. 3. Polarization-angle-dependent SHG and fitting. Using higher excitation energies ($2 \times E_L = 2.1$) eV for (a) HS1, (b) HS2, and (c) HS3. Experimental points are presented with magenta spheres and the fitting of the total SHG signal is shown in green lines. The twist angle values θ_t used in Eq. (1) for the total fit are the experimental values 29.8°, 4.3°, and 0.8° for HS1, HS2, and HS3, respectively. The amplitude ratio $L_1(MoS_2)$:$L_2(WSe_2)$ is 1.5, 1, and 0.6, while the phase, φ, is kept at 79° in all cases. The SHG modulation of the individual layers that construct the total SHG is shown in black and blue lines for MoS_2 and WSe_2, respectively. For HS1 (a) where there is a finite minimum to maximum ratio due to the phase shift and large twist angle, a fitting with zero phase shift is shown as a dashed red line for comparison.

three-dimensional buckling [59]. Furthermore, using the same approach as Refs. [47,62,71], we find that the second-order sheet susceptibility, $\chi_{sh}^{(2)}$, and SHG power on the A-exciton resonances of the three heterostructures are on the order of 10^{-20} m^2/V and tens of femtowatts, respectively (see Supplemental Material B for comparison of $\chi_{sh}^{(2)}$ values [61]). However, in the case of aligned MoS_2/WSe_2 heterostructures (HS3), a noticeable decrease of $\chi_{sh}^{(2)}$ is observed, possibly due to partial transfer of the oscillator strength from intralayer A-exciton states to hybridized/moiré states [14].

Second, we analyze the main experimental findings for the samples with nonzero twist angle, HS1 and HS2. The main observations are linearly polarized SHG for the specific case of $2 \times E_L$ in resonance with the intralayer exciton resonances, where the polarization axis is aligned with the armchair direction of the monolayer whose exciton resonance was addressed. We then show that at higher laser energies the SHG from the heterostructure is elliptically polarized for HS1 and close to linearly polarized for HS2, with a polarization axis away from the monolayer orientations.

An interesting analysis of SHG from *homobilayers* with different twist angle is given in Ref. [39]. The situation is more complex in *heterobilayers*, where both monolayers have finite, yet different, contributions in the total SHG signal, as discussed in Ref. [43]. As a result, the minimum to maximum SHG signal ratio (i.e., minor to major axial ratio of polarization, ρ) can change considerably for large twist angles [e.g., see Fig. 3(a)]. The combination of a phase difference between the two fields and a finite twist angle introduce an elliptical polarization in the total field [70]. To go further in our analysis, we adopt the simple approach proposed in Ref. [43] based on the interference of plane waves, which does not explicitly include any layer hybridization. In a PSHG experiment on a heterobilayer, the parallel component of the SHG signal can be expressed as

$$I_P = L_1^2 \cos^2(3\vartheta) + L_2^2 \cos^2[3(\theta_t - \vartheta)] + 2L_1 L_2 \cos(3\vartheta) \cos[3(\theta_t - \vartheta)] \cos\varphi, \quad (1)$$

where L_1 and L_2 are the SHG amplitudes of the first and second monolayer, ϑ is the relative angle between the fundamental (laser) polarization and the armchair direction of the monolayer, θ_t is the twist angle, and φ is the phase difference between the two SHG fields. In our experiment we vary ϑ by rotating a superachromatic half-wave plate (see Supplemental Material C for experimental details [61]).

In the experiments presented here, we bring together very specific conditions that allow us to vary SHG signals from a heterobilayer described by Eq. (1).

(i) We use a diffraction-limited detection/excitation spot size, so we can compare monolayer and heterostructure response without spatial overlap as the spot size is smaller than the lateral dimensions of the sample regions.

(ii) Our tunable source is a picosecond laser and has a narrow spectral FWHM of typically 4 meV.

(iii) We perform experiments at low temperature in high-quality hBN encapsulated structures, which results in spectrally narrow (few meV FWHM) exciton transition linewidth [72] (see Supplemental Material A for photoluminescence spectra [61]) and allows us to address individual optical resonances in the two layers.

(iv) A-exciton resonances in WSe_2 and MoS_2 lie spectrally 200 meV apart, allowing us to target them separately.

By carefully adjusting experimental parameters (i) to (iv) we can control the SHG signal of the heterostructure. *Linear polarization* of the SHG signal from the heterobilayer can occur for several configurations.

(1) Linear polarization can occur by tuning the $2 \times E_L$ into resonance with the A-exciton state of one of the two monolayers. Then, independently of the twist angle, I_P reduces to a single $\cos^2(3\theta)$ term since the SHG from the selected monolayer will dominate and either L_1 or L_2 are zero in Eq. (1). This allows us to describe the results in Figs. 2(e) and 2(f) and also in Fig. 1(g).

(2) At energies where both monolayers contribute to the SHG signal (i.e., both L_1 and $L_2 \neq 0$) and for nonzero twist angles, linear polarization occurs if the phase difference $\varphi = 0$ [see red dashed curve in Fig. 3(a)].

(3) In the case of aligned heterostructures (see HS3 with $\theta_t \simeq 0^\circ$) the polarization of the total SHG field is always linear.

In order to generate *elliptical polarization* as observed for HS1, both the twist angle θ_t and the phase shift φ need to be nonzero in Eq. (1). In the polarization-dependent plots, as a function of ϑ in Fig. 3(a) elliptical polarization results in a different ρ. For instance, in HS1 the twist angle is large ($\approx 30^\circ$) and the minimum to major axial ratio is 1 order of magnitude different when we compare $2 \times E_L = 1.92$ eV [Fig. 2(d), $\rho \simeq 0.03$:1] with respect to $2 \times E_L = 2.1$ eV [Fig. 3(a), $\rho \simeq 0.39$:1]. For the fits in Figs. 3(a)–3(c) based on Eq. (1) we use the twist angle determined beforehand for each HS. We treat the amplitudes L_1 and L_2 and the phase φ as fitting parameters in HS1 and then we use the same phase for HS2 and HS3; the results are summarized in the caption of Fig. 3. Our target here is not to quantify the phase φ, but to demonstrate that the total SHG signal from a twisted heterostructure can be either linearly or elliptically polarized, depending on whether both monolayers contribute to the overall signal. Spectral phase interferometry can be employed to measure φ, as has been demonstrated elsewhere (see Ref. [43]). The *elliptical polarization* we experimentally obtain for HS1 at $2 \times E_L = 2.1$ eV indicates exciton resonances from either layer at this energy which have a different phase [73]. This could possibly be explained by different contributions from intralayer B excitons of WSe_2 and MoS_2 monolayers at this energy [74–76].

For small and close to zero twist angles of HS2 and HS1 the experimentally measured polarization of the SH is close to linear as expected from Eq. (1), so fit parameters are not uniquely defined, as varying the amplitude ratio and the phase has numerically the same effect on the overall polarization and amplitude.

IV. CONCLUSIONS

We have performed PSHG spectroscopy in MoS_2/WSe_2 heterostructures. Tuning twice the excitation energy in resonance with an intralayer excitonic transition of the constituent monolayers allows the *in situ* determination (directly on the heterostructure) of the twist angle. This is a consequence of

the SHG amplitude and polarization control by addressing energetically distinct intralayer exciton resonances in the top and bottom layers. This approach can be applied to a large number of heterobilayer systems [1]. We conclude that the total SHG intensity and polarization for a given TMD heterostructure depend on (i) the twist angle, (ii) the relative amplitude between the SH fields of the constituent monolayers at a given excitation energy, and (iii) the phase difference between the SH waves. Finally, we show in SHG spectroscopy that the band structure of aligned (close to 0°) MoS_2/WSe_2 heterostructures is strongly altered as compared to samples with larger twist angles. We observe considerable shifts of exciton resonance energies and the appearance of new resonances in the linear and nonlinear susceptibilities.

V. METHODS

Sample. See Supplemental Material A for an optical microscope image of the sample [61]. An exfoliated monolayer MoS_2 with large lateral size (≈120 μm, blue dashed lines) lies on top of an ≈150-nm-thick hBN, while three different exfoliated WSe_2 monolayers (red dashed lines) are deliberately transferred on top of MoS_2 in different twist angles after alignment of the long edges of the flakes. As a result, three different heterostructures are formed, namely, HS1, HS2, and HS3. In all cases, there is optical access to the bare monolayers to confirm the validity of the results collected from the heterostructures. The same thin (≈10 nm) top hBN covers the whole structure. The uniformity of the top and bottom hBN thicknesses is important because thin-film interference effects can modify the SHG intensity and the reflectivity shape/amplitude when comparing different samples. We measure differential reflectivity $\Delta R/R = (R_{\mathrm{TMD}} - R_{\mathrm{sub}})/R_{\mathrm{sub}}$, where R_{TMD} is the intensity reflection coefficient of the TMD heterostructure (or the monolayer) and R_{sub} is the reflection coefficient of the hBN/SiO_2 stack. The overall shape of the differential reflectivity spectrum depends on cavity effects (thin layer interference) given by the top and bottom hBN and SiO_2 thicknesses. As a result, the exciton transition line shape varies in amplitude and sign in the presented spectra [75].

For SHG measurements, we use pulses with a pulse duration of 1 ps. The pulses are generated by a tunable optical parametric oscillator synchronously pumped by a mode-locked Ti:sapphire laser. The SHG signal is collected in reflection geometry, while before any spectral acquisition the pulse duration and the spectral shape of the fundamental are monitored for every different wavelength by an autocorrelator and a wave meter. In addition, the average power of the fundamental is adjusted according to a power meter, normalized to each wavelength. This allows us to directly compare the measurements from different samples. For the polarization-resolved SHG experiments a superachromatic Thorlabs SAHWP05M-1700 half-lambda wave plate was used; the error in retardance within the wavelength range studied here is smaller than 0.1%.

ACKNOWLEDGMENTS

Toulouse acknowledges funding from ANR 2D-vdW-Spin, ANR MagicValley, ANR IXTASE, ANR ATOEMS, and the Institut Universitaire de France. Growth of hexagonal boron nitride crystals was supported by JSPS KAKENHI (Grants No. 19H05790, No. 20H00354 and No. 21H05233).

[1] K. Tran, J. Choi, and A. Singh, 2D Mater. **8**, 022002 (2021).
[2] S. Shree, I. Paradisanos, X. Marie, C. Robert, and B. Urbaszek, Nat. Rev. Phys. **3**, 39 (2021).
[3] G. Oster and Y. Nishijima, Sci. Am. **208**, 54 (1963).
[4] H. Yu, G.-B. Liu, J. Tang, X. Xu, and W. Yao, Sci. Adv. **3**, e1701696 (2017).
[5] Y. Cao, V. Fatemi, S. Fang, K. Watanabe, T. Taniguchi, E. Kaxiras, and P. Jarillo-Herrero, Nature (London) **556**, 43 (2018).
[6] Y. Shimazaki, I. Schwartz, K. Watanabe, T. Taniguchi, M. Kroner, and A. Imamoğlu, Nature (London) **580**, 472 (2020).
[7] Y. Xu, S. Liu, D. A. Rhodes, K. Watanabe, T. Taniguchi, J. Hone, V. Elser, K. F. Mak, and J. Shan, Nature (London) **587**, 214 (2020).
[8] L. An, X. Cai, D. Pei, M. Huang, Z. Wu, Z. Zhou, J. Lin, Z. Ying, Z. Ye, X. Feng *et al.*, Nanoscale Horiz. **5**, 1309 (2020).
[9] T. I. Andersen, G. Scuri, A. Sushko, K. De Greve, J. Sung, Y. Zhou, D. S. Wild, R. J. Gelly, H. Heo, D. Bérubé *et al.*, Nat. Mater. **20**, 480 (2021).
[10] A. R.-P. Montblanch, D. M. Kara, I. Paradisanos, C. M. Purser, M. S. Feuer, E. M. Alexeev, L. Stefan, Y. Qin, M. Blei, G. Wang *et al.*, Commun. Phys. **4**, 119 (2021).
[11] P. Rivera, H. Yu, K. L. Seyler, N. P. Wilson, W. Yao, and X. Xu, Nat. Nanotechnol. **13**, 1004 (2018).
[12] K. L. Seyler, P. Rivera, H. Yu, N. P. Wilson, E. L. Ray, D. G. Mandrus, J. Yan, W. Yao, and X. Xu, Nature (London) **567**, 66 (2019).
[13] H. Baek, M. Brotons-Gisbert, Z. Koong, A. Campbell, M. Rambach, K. Watanabe, T. Taniguchi, and B. Gerardot, Sci. Adv. **6**, eaba8526 (2020).
[14] E. M. Alexeev, D. A. Ruiz-Tijerina, M. Danovich, M. J. Hamer, D. J. Terry, P. K. Nayak, S. Ahn, S. Pak, J. Lee, J. I. Sohn *et al.*, Nature (London) **567**, 81 (2019).
[15] Y. Tang, J. Gu, S. Liu, K. Watanabe, T. Taniguchi, J. Hone, K. F. Mak, and J. Shan, Nat. Nanotechnol. **16**, 52 (2021).
[16] L. Zhang, Z. Zhang, F. Wu, D. Wang, R. Gogna, S. Hou, K. Watanabe, T. Taniguchi, K. Kulkarni, T. Kuo *et al.*, Nat. Commun. **11**, 5888 (2020).
[17] I. Paradisanos, S. Shree, A. George, N. Leisgang, C. Robert, K. Watanabe, T. Taniguchi, R. J. Warburton, A. Turchanin, X. Marie *et al.*, Nat. Commun. **11**, 2391 (2020).
[18] Z. Wang, D. A. Rhodes, K. Watanabe, T. Taniguchi, J. C. Hone, J. Shan, and K. F. Mak, Nature (London) **574**, 76 (2019).
[19] L. Sigl, F. Sigger, F. Kronowetter, J. Kiemle, J. Klein, K. Watanabe, T. Taniguchi, J. J. Finley, U. Wurstbauer, and A. W. Holleitner, Phys. Rev. Research **2**, 042044(R) (2020).
[20] C. Lagoin and F. Dubin, Phys. Rev. B **103**, L041406 (2021).
[21] R. W. Boyd, *Nonlinear Optics* (Academic, San Diego, 2020).

[22] P. A. Franken, A. E. Hill, C. W. Peters, and G. Weinreich, Phys. Rev. Lett. **7**, 118 (1961).

[23] R. W. Terhune, P. D. Maker, and C. M. Savage, Phys. Rev. Lett. **8**, 404 (1962).

[24] A. Yariv and P. Yeh, *Photonics: Optical Electronics in Modern Communications*, 6th ed. (Oxford University, New York, 2006).

[25] M. Lafrentz, D. Brunne, A. V. Rodina, V. V. Pavlov, R. V. Pisarev, D. R. Yakovlev, A. Bakin, and M. Bayer, Phys. Rev. B **88**, 235207 (2013).

[26] S. Bergfeld and W. Daum, Phys. Rev. Lett. **90**, 036801 (2003).

[27] D. R. Yakovlev, V. V. Pavlov, A. V. Rodina, R. V. Pisarev, J. Mund, W. Warkentin, and M. Bayer, Phys. Solid State **60**, 1471 (2018).

[28] X. Lu, G. Moille, A. Rao, D. A. Westly, and K. Srinivasan, Nat. Photonics **15**, 131 (2021).

[29] Z. Sun, Y. Yi, T. Song, G. Clark, B. Huang, Y. Shan, S. Wu, D. Huang, C. Gao, Z. Chen *et al.*, Nature (London) **572**, 497 (2019).

[30] F. J. Löchner, R. Mupparapu, M. Steinert, A. George, Z. Tang, A. Turchanin, T. Pertsch, I. Staude, and F. Setzpfandt, Opt. Express **27**, 35475 (2019).

[31] R. Cunha, A. Cadore, S. L. Ramos, K. Watanabe, T. Taniguchi, S. Kim, A. S. Solntsev, I. Aharonovich, and L. M. Malard, J. Phys.: Condens. Matter **32**, 19LT01 (2020).

[32] K. L. Seyler, J. R. Schaibley, P. Gong, P. Rivera, A. M. Jones, S. Wu, J. Yan, D. G. Mandrus, W. Yao, and X. Xu, Nat. Nanotechnol. **10**, 407 (2015).

[33] G. Wang, X. Marie, I. Gerber, T. Amand, D. Lagarde, L. Bouet, M. Vidal, A. Balocchi, and B. Urbaszek, Phys. Rev. Lett. **114**, 097403 (2015).

[34] K.-Q. Lin, S. Bange, and J. M. Lupton, Nat. Phys. **15**, 242 (2019).

[35] L. Mennel, M. M. Furchi, S. Wachter, M. Paur, D. K. Polyushkin, and T. Mueller, Nat. Commun. **9**, 516 (2018).

[36] L. De Dominicis, S. Botti, L. S. Asilyan, R. Ciardi, R. Fantoni, M. L. Terranova, A. Fiori, S. Orlanducci, and R. Appolloni, Appl. Phys. Lett. **85**, 1418 (2004).

[37] I. Abdelwahab, G. Grinblat, K. Leng, Y. Li, X. Chi, A. Rusydi, S. A. Maier, and K. P. Loh, ACS Nano **12**, 644 (2018).

[38] M. Fiebig, D. Frohlich, S. Leute, and R. V. Pisarev, J. Appl. Phys. **83**, 6560 (1998).

[39] W.-T. Hsu, Z.-A. Zhao, L.-J. Li, C.-H. Chen, M.-H. Chiu, P.-S. Chang, Y.-C. Chou, and W.-H. Chang, ACS Nano **8**, 2951 (2014).

[40] T. Jiang, H. Liu, D. Huang, S. Zhang, Y. Li, X. Gong, Y.-R. Shen, W.-T. Liu, and S. Wu, Nat. Nanotechnol. **9**, 825 (2014).

[41] S. Psilodimitrakopoulos, L. Mouchliadis, I. Paradisanos, G. Kourmoulakis, A. Lemonis, G. Kioseoglou, and E. Stratakis, Sci. Rep. **9**, 1 (2019).

[42] K.-Q. Lin, P. E. F. Junior, J. M. Bauer, B. Peng, B. Monserrat, M. Gmitra, J. Fabian, S. Bange, and J. M. Lupton, Nat. Commun. **12**, 1553 (2021).

[43] W. Kim, J. Y. Ahn, J. Oh, J. H. Shim, and S. Ryu, Nano Lett. **20**, 8825 (2020).

[44] S. Psilodimitrakopoulos, L. Mouchliadis, G. M. Maragkakis, G. Kourmoulakis, A. Lemonis, G. Kioseoglou, and E. Stratakis, 2D Mater. **8**, 015015 (2020).

[45] J. E. Zimmermann, Y. D. Kim, J. C. Hone, U. Höfer, and G. Mette, Nanoscale Horiz. **5**, 1603 (2020).

[46] X. Wen, Z. Gong, and D. Li, InfoMat **1**, 317 (2019).

[47] S. Klimmer, O. Ghaebi, Z. Gan, A. George, A. Turchanin, G. Cerullo, and G. Soavi, Nat. Photon. **15**, 837 (2021).

[48] J. R. Schaibley, P. Rivera, H. Yu, K. L. Seyler, J. Yan, D. G. Mandrus, T. Taniguchi, K. Watanabe, W. Yao, and X. Xu, Nat. Commun. **7**, 13747 (2016).

[49] C. Jin, E. C. Regan, A. Yan, M. I. B. Utama, D. Wang, S. Zhao, Y. Qin, S. Yang, Z. Zheng, S. Shi *et al.*, Nature (London) **567**, 76 (2019).

[50] A. Weston, Y. Zou, V. Enaldiev, A. Summerfield, N. Clark, V. Zólyomi, A. Graham, C. Yelgel, S. Magorrian, M. Zhou *et al.*, Nat. Nanotechnol. **15**, 592 (2020).

[51] S. Carr, D. Massatt, S. B. Torrisi, P. Cazeaux, M. Luskin, and E. Kaxiras, Phys. Rev. B **98**, 224102 (2018).

[52] Y. Pan, S. Folsch, Y. Nie, D. Waters, Y.-C. Lin, B. Jariwala, K. Zhang, K. Cho, J. A. Robinson, and R. M. Feenstra, Nano Lett. **18**, 1849 (2018).

[53] J. Kunstmann, F. Mooshammer, P. Nagler, A. Chaves, F. Stein, N. Paradiso, G. Plechinger, C. Strunk, C. Schüller, G. Seifert *et al.*, Nat. Phys. **14**, 801 (2018).

[54] O. Karni, E. Barré, S. C. Lau, R. Gillen, E. Y. Ma, B. Kim, K. Watanabe, T. Taniguchi, J. Maultzsch, K. Barmak, R. H. Page, and T. F. Heinz, Phys. Rev. Lett. **123**, 247402 (2019).

[55] C. Zhang, C.-P. Chuu, X. Ren, M.-Y. Li, L.-J. Li, C. Jin, M.-Y. Chou, and C.-K. Shih, Sci. Adv. **3**, e1601459 (2017).

[56] O. Karni, E. Barré, V. Pareek, J. D. Georgaras, M. K. Man, C. Sahoo, D. R. Bacon, X. Zhu, H. B. Ribeiro, A. L. O'Beirne *et al.*, arXiv:2108.01933.

[57] K. Yao, N. R. Finney, J. Zhang, S. L. Moore, L. Xian, N. Tancogne-Dejean, F. Liu, J. Ardelean, X. Xu, D. Halbertal *et al.*, Sci. Adv. **7**, eabe8691 (2021).

[58] D. Waters, Y. Nie, F. Lüpke, Y. Pan, S. Fölsch, Y.-C. Lin, B. Jariwala, K. Zhang, C. Wang, H. Lv *et al.*, ACS Nano **14**, 7564 (2020).

[59] H. Li, S. Li, M. H. Naik, J. Xie, X. Li, J. Wang, E. Regan, D. Wang, W. Zhao, S. Zhao *et al.*, Nat. Mater. **20**, 945 (2021).

[60] C. Cho, J. Wong, A. Taqieddin, S. Biswas, N. R. Aluru, S. Nam, and H. A. Atwater, Nano Lett. **21**, 3956 (2021).

[61] See Supplemental Material at http://link.aps.org/supplemental/10.1103/PhysRevB.105.115420 which contains additional information on experimental methods, second-order susceptibility, and polarization resolved SHG.

[62] S. Shree, D. Lagarde, L. Lombez, C. Robert, A. Balocchi, K. Watanabe, T. Taniguchi, X. Marie, I. C. Gerber, M. M. Glazov *et al.*, Nat. Commun. **12**, 6894 (2021).

[63] I. C. Gerber, E. Courtade, S. Shree, C. Robert, T. Taniguchi, K. Watanabe, A. Balocchi, P. Renucci, D. Lagarde, X. Marie, and B. Urbaszek, Phys. Rev. B **99**, 035443 (2019).

[64] G. Wang, I. Gerber, L. Bouet, D. Lagarde, A. Balocchi, M. Vidal, T. Amand, X. Marie, and B. Urbaszek, 2D Mater. **2**, 045005 (2015).

[65] M. M. Glazov, L. E. Golub, G. Wang, X. Marie, T. Amand, and B. Urbaszek, Phys. Rev. B **95**, 035311 (2017).

[66] M. Zhao, Z. Ye, R. Suzuki, Y. Ye, H. Zhu, J. Xiao, Y. Wang, Y. Iwasa, and X. Zhang, Light Sci. Appl. **5**, e16131 (2016).

[67] L. Lafeta, A. Corradi, T. Zhang, E. Kahn, I. Bilgin, B. R. Carvalho, S. Kar, M. Terrones, and L. M. Malard, 2D Mater. **8**, 035010 (2021).

[68] Y. Li, Y. Rao, K. F. Mak, Y. You, S. Wang, C. R. Dean, and T. F. Heinz, Nano Lett. **13**, 3329 (2013).

[69] X. Hong, J. Kim, S.-F. Shi, Y. Zhang, C. Jin, Y. Sun, S. Tongay, J. Wu, Y. Zhang, and F. Wang, Nat. Nanotechnol. **9**, 682 (2014).

[70] E. Hecht, *Optics* (Pearson Education Limited, Harlow, England, 2017).

[71] R. Woodward, R. Murray, C. Phelan, R. De Oliveira, T. Runcorn, E. Kelleher, S. Li, E. De Oliveira, G. Fechine, G. Eda *et al.*, 2D Mater. **4**, 011006 (2016).

[72] F. Cadiz, E. Courtade, C. Robert, G. Wang, Y. Shen, H. Cai, T. Taniguchi, K. Watanabe, H. Carrere, D. Lagarde, M. Manca, T. Amand, P. Renucci, S. Tongay, X. Marie, and B. Urbaszek, Phys. Rev. X **7**, 021026 (2017).

[73] R. Chang, J. Ducuing, and N. Bloembergen, Phys. Rev. Lett. **15**, 6 (1965).

[74] A. Kormányos, G. Burkard, M. Gmitra, J. Fabian, V. Zólyomi, N. D. Drummond, and V. Falko, 2D Mater. **2**, 022001 (2015).

[75] C. Robert, M. A. Semina, F. Cadiz, M. Manca, E. Courtade, T. Taniguchi, K. Watanabe, H. Cai, S. Tongay, B. Lassagne, P. Renucci, T. Amand, X. Marie, M. M. Glazov, and B. Urbaszek, Phys. Rev. Materials **2**, 011001(R) (2018).

[76] A. V. Stier, N. P. Wilson, K. A. Velizhanin, J. Kono, X. Xu, and S. A. Crooker, Phys. Rev. Lett. **120**, 057405 (2018).